Rising Speed Limits for Fluxons via Edge-Quality Improvement in Wide MoSi Thin Films

B. Budinská,[1,2,*] B. Aichner,[1,2] D. Yu. Vodolazov,[3] M. Yu. Mikhailov,[4] F. Porrati,[5] M. Huth,[5] A.V. Chumak,[1] W. Lang,[1] and O.V. Dobrovolskiy[1,†]

[1] *Faculty of Physics, University of Vienna, 1090 Vienna, Austria*

[2] *University of Vienna, Vienna Doctoral School in Physics, 1090 Vienna, Austria*

[3] *Institute for Physics of Microstructures, Russian Academy of Sciences, Nizhny Novgorod region 603087, Russia*

[4] *B. Verkin Institute for Low Temperature Physics and Engineering, National Academy of Sciences of Ukraine, 61103 Kharkiv, Ukraine*

[5] *Physikalisches Institut, Goethe University, 60438 Frankfurt am Main, Germany*

(Received 26 November 2021; revised 27 January 2022; accepted 25 February 2022; published 30 March 2022)

Ultrafast vortex motion has recently become a subject of extensive investigations, triggered by the fundamental question regarding the ultimate speed limits for magnetic flux quanta and enhancements of single-photon detectors. In this regard, the current-biased quench of a dynamic flux-flow regime—flux-flow instability (FFI)—has turned into a widely used method for the extraction of information about the relaxation of quasiparticles (unpaired electrons) in a superconductor. However, the large relaxation times τ_ϵ deduced from FFI for many superconductors are often inconsistent with the fast relaxation processes implied by their single-photon counting capability. Here, we investigate FFI in 15-nm-thick 182-μm-wide MoSi strips with rough and smooth edges produced by laser etching and milling by a focused ion beam. For the strip with smooth edges we deduce, from current-voltage (I-V) curve measurements, a factor of 3 larger critical currents I_c, a factor of 20 higher maximal vortex velocities of 20 km/s, and a factor of 20 shorter τ_ϵ. We argue that for the deduction of the intrinsic τ_ϵ of the material from the I-V curves, utmost care should be taken regarding the edge and sample quality and such a deduction is justified only if the field dependence of I_c points to the dominating edge pinning of vortices.

DOI: 10.1103/PhysRevApplied.17.034072

I. INTRODUCTION

Ultrafast vortex motion in superconductors has recently attracted great attention both experimentally [1–6] and theoretically [7–12]. This attention is triggered by the fundamental question regarding the ultimate speed limit for magnetic flux transport via superconducting vortices and the phenomena of generation of sound [13,14] and spin waves [15,16] by fluxons moving at velocities of a few kilometers per second. Furthermore, high-velocity vortex dynamics is essential for the photoresponse of superconductor microstrip single-photon detectors (SMSPDs). Operated at large bias currents [17–20], which enable a vortex-assisted mechanism of single-photon counting [21], such microstrips appear as viable candidates for various applications requiring large-area detectors, e.g., free-space quantum cryptography, deep space optical communication, etc. If a SMSPD is capable of carrying a close-to-depairing transport current, its intrinsic detection efficiency is predicted to reach almost 100% [21]. Thus, materials with large critical currents are in demand for SMSPDs and require the understanding of vortex matter under far-from-equilibrium conditions. In this regard, current-biased quenches of the dynamic flux-flow regime provide a way for the extraction of information about the relaxation of quasiparticles (unpaired electrons) [4] in a superconductor. The deduced quasiparticle relaxation times are then often used for judging whether a material could be potentially suitable for use in single-photon detectors [5,22–25].

The physical phenomenon underlying this judgment is known as the flux-flow instability (FFI) [1–12,22–25]. FFI occurs in the regime of fast vortex motion and, in the current-driven regime, it becomes apparent as a sudden jump to a highly resistive state in the current-voltage (I-V) curve of the superconductor. Microscopically, FFI is associated with the diffusion of quasiparticles from the

*barbora.budinska@univie.ac.at

†oleksandr.dobrovolskiy@univie.ac.at

vortex cores to the surrounding superconducting medium, and the subsequent retrapping of the quasiparticles by other vortices. According to Larkin and Ovchinnikov (LO) [26–28], close to the superconducting transition temperature T_c, the maximal vortex velocity (instability velocity) v^* is linked with the quasiparticle energy relaxation time τ_ϵ via the expression $v^* = \{D[14\zeta(3)]^{1/2}(1 - T/T_c)^{1/2}/(\pi\tau_\epsilon)\}^{1/2}$, where D is the electron diffusion coefficient and $\zeta(x)$ is the Riemann zeta function. This LO expression suggests that materials with shorter τ_ϵ should, in principle, allow for higher vortex velocities. The essential assumptions in the LO theory [26,27] are (i) the perfect periodicity of the vortex lattice, (ii) the absence of defects and edges in the superconductor, and (iii) neglect of heating effects associated with the Joule dissipation. Accordingly, the LO theory can take into account neither collective effects leading to the dynamic transformation of the vortex lattice nor vortex-pinning and edge-barrier effects. In subsequent studies, however, it was revealed that larger v^* can be realized in materials with a weak uncorrelated disorder [29–31], via the vortex guiding effect [3] or via addition of a gigahertz-frequency ac current to the dc bias current [32]. At the same time, in a uniform system, the highest vortex velocities were experimentally observed in a direct-write Nb-C superconductor with a small diffusion coefficient and fast relaxation of quasiparticles ($\tau_\varepsilon \simeq$ 20 ps) [5] and in bridges of lead [1], which has a large diffusion coefficient and a short inelastic electron-phonon relaxation time ($\tau_{e\text{-ph}} \simeq 20$ ps) [33]. Remarkably, while many dirty superconductors (NbN [34], MoSi [18], NbRe [35], NbReN [25], etc.) possess good single-photon detection capability, v^* and τ_ϵ deduced from FFI are not always consistent with the fast relaxation processes implied by photon-counting experiments. For instance, the deduced v^* values of approximately 1 m/s for α-MoSi [24,36], 0.1–0.5 km/s for MoSi [37], 0.2 km/s for NbN [38], and 0.3–0.7 km/s for β-W and NbReN [23,25] yield τ_ϵ on the (sub-)nanosecond time scale.

Recently, it was predicted theoretically and confirmed experimentally that FFI does not necessarily occur in the entire volume of a sample, but it can have a local character [8]. If the sample is inhomogeneous, then in the flux-flow regime it could be that regions with slower- and faster-moving vortices coexist, leading to the formation of normally conducting domains in the regions where v^* is reached first. Once the current density exceeds some threshold current density (determining the equilibrium of the nonisothermal normal-superconducting boundary) [39,40] these domains begin to grow and the whole sample transits to the normal state [8]. In this case, the standard relation $v^* = V^*/(BL)$ (V^*, measured voltage just before the transition; B, magnitude of the applied magnetic field; L, distance between the voltage leads) can no longer yield the instability velocity quantitatively. Nevertheless, the functional relations between the LO instability parameters in the case of a local FFI remain the same as in the case of a global FFI, but require renormalization of the sample length [8]. At the same time, it is worth noting that regardless of the FFI character, the places where FFI is actually nucleating are determined by defects at that edge through which vortices enter the sample [7]. Microscopically, such defects affect the vortex motion primarily via the local suppression of the edge barrier for vortex entry either due to variation of material parameters (critical temperature, electron mean free path, etc.) or due to the local enhancement of the transport current density (current-crowding effect) near geometrical defects [41–46].

Here, we compare the nonequilibrium state generated by vortex motion in MoSi strips with focused-ion-beam (FIB)-milled and laser-etched edges. We choose MoSi because it is known for its very weak intrinsic pinning and as a material that is promising for single-photon detectors [18,19,47,48]. Specifically, for MoSi strips with smooth edges milled by a FIB we reveal that the critical current I_c is controlled by the edge barrier in a wide range of magnetic fields and I_c is close to the depairing current I_{dep} at $B = 0$, which is indicative of a high homogeneity of the material. From the I-V curves we deduce instability velocities v^* in the 5–20-km/s range and energy relaxation times τ_ϵ on the 30-ps time scale. By contrast, in the laser-etched MoSi strip, I_c is several times smaller than I_{dep}, $I_c(B)$ does not show indications for edge-barrier effects, and the v^* values are an order of magnitude smaller and close to the values deduced in the past for MoSi [36,37] and other dirty superconductor films [23,24,38]. We explain these differences by the change in the quality of the close-to-edge regions by the laser etching process, which leads to a strong local inhomogeneity, bulk pinning, and, thus, to a much lower instability velocity. Our results imply that for strips where no care is taken about the edge quality and bulk homogeneity, and whose magnetic field dependence of the critical current does not attest to the dominating edge-barrier effect, FFI only allows for the deduction of some "indicative" relaxation time exceeding the intrinsic τ_ϵ in the material.

II. EXPERIMENT

The nonequilibrium state generated by fast vortex motion is investigated for two 15-nm-thick amorphous superconducting MoSi strips differing by edge roughness. The experimental geometry is shown in Fig. 1(a). The MoSi films are deposited by dc magnetron cosputtering of elemental molybdenum and silicon targets onto Si wafers covered with a thermally grown 230-nm-thick SiO_2 layer. The $Mo_{70}Si_{30}$ composition of the films is ensured by using calibrated deposition rates and inspection of thicker film replica by energy-dispersive x-ray (EDX) spectroscopy. The films are deposited onto 5-nm-thick Si buffer

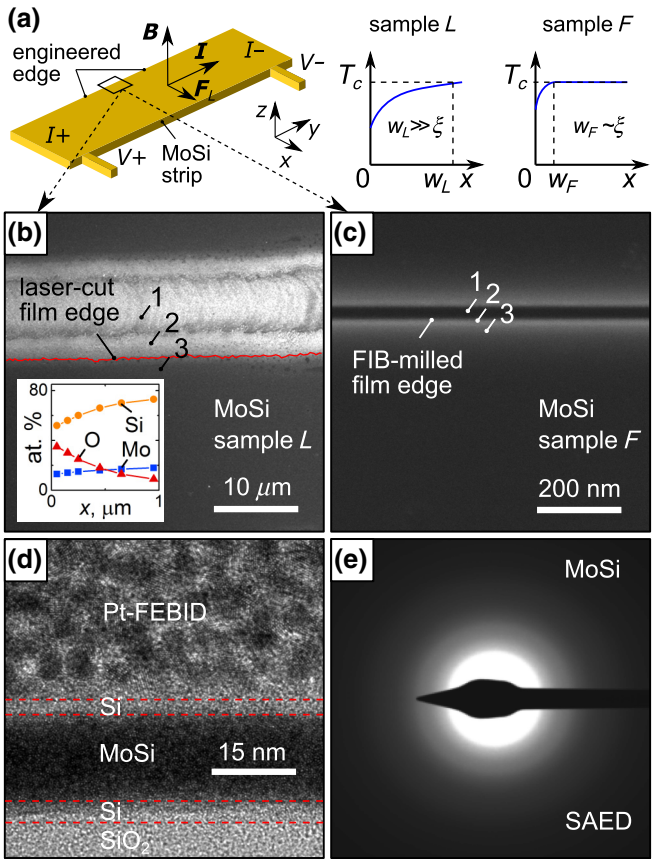

FIG. 1. (a) Experimental geometry. The different quality of the edges creates different conditions for the entry of Abrikosov vortices into the strips. SEM images of the film regions near the edges formed by (b) laser-beam etching and (c) focused-ion-beam milling. The laser-etched edge is rough (red line) in (b) while the FIB-milled edge is smooth in (c). Note the different scale in (b),(c). Inset in (b): material composition near the edge ($x = 0$) in sample L. (d) TEM image and (e) selected area electron diffraction pattern of the MoSi film.

layers and covered with 3-nm-thick Si layers for protection against oxidation. The films have a flat morphology, with a rms surface roughness of less than 0.1 nm, as deduced from atomic force microscopy (AFM) scans in the range $1 \times 1\ \mu m^2$. Microstructural characterization of MoSi lamellas by transmission electron microscopy (TEM; Tecnai F30, 300 kV) reveals high structural uniformity of the films [see Fig. 1(d)]. An exemplary selected area electron diffraction pattern of the MoSi film is shown in Fig. 1(e). The absence of diffraction rings in Fig. 1(e) attests to an amorphous microstructure of the material, in contrast with various polycrystalline microstructures [49,50].

For electrical resistance measurements the films are patterned into a four-probe geometry, with a strip length $L = 616\ \mu m$ and width $W = 182\ \mu m$. One strip is etched out by laser beam (sample L) and another strip by Ga FIB milling (sample F). The use of different patterning techniques allows for the realization of rough and smooth edges, respectively [see also Figs. 1(b) and 1(c)].

Laser etching is done under ambient conditions using an LGI-505 gas laser source, with 337-nm wavelength, 7-ns pulse duration and up to 1000 pulses per second of the laser. The beam power, focal spot size, and speed of beam rastering are decisive for the edge quality. These parameters are adjusted to produce an edge shown in Fig. 1(b). The discrete spatial character of the laser beam impact is seen as a circle-footprint contrast variation along the groove etched in the substrate [region 1 in Fig. 1(b)]. Gaussian flanks of the laser beam, with a focal spot diameter of about 6 μm, cause evaporation of the MoSi film within a region of width 2–3 μm along the edge (region 2). As a result, an irregular, saw-tooth-like strip edge profile [red thin line in Fig. 1(b)] is created in sample L, characterized by an irregular variation of the edge barrier for vortex entry into the interior of the strip (region 3). The variation of the composition of sample L induced by the laser etching process within a region of width $w_L \simeq 1\ \mu m$ along the edge is shown in the inset of Fig. 1(b). The local film composition is inferred from EDX spectroscopy at 5 kV (1.6 nA) for a series of $100 \times 100\ nm^2$ areas probed at different distances from the strip edge. The larger oxygen content in the close-to-edge region leads to a degradation of the superconducting properties. The larger relative contents of Si and O with respect to the $Mo_{70}Si_{30}$ composition are because of the significantly larger thickness (of about 90 nm) of the layer probed by 5-kV electrons than the film thickness.

FIB milling is done in a dual-beam scanning electron microscope (SEM; FEI Nova NanoLab 600) at 30 kV (30 pA) and 20-nm pitch. The milling of a groove [region 1 in Fig. 1(c)] is accompanied by stopping of Ga ions within a region of width $w_F \sim 10$ nm along the edges in sample F, as inferred from stopping and range of ions in matter simulations and seen as a lighter region 2 in the SEM image in Fig. 1(c). The rms edge roughness in the y direction is less than 0.5 nm, as deduced from an AFM scan over a distance of 500 nm along the edge. Thus, the edges of sample F produce a close-to-perfect edge barrier for vortex entry into the strip (region 3).

Electrical resistance measurements are done in a He bath cryostat equipped with a superconducting solenoid. Magnetic field is applied perpendicular to the strip plane and the I-V curves are recorded in the current-driven regime. The temperature dependence of the resistance exhibits a weak localization behavior [see Fig. 2(a), which is representative for both samples], with a resistivity of $\rho_{7K} \approx 148\ \mu\Omega\,cm$ at 7 K. Figure 2(b) depicts the superconducting transition of the MoSi film at $T_c = 6.43$ K, as determined by using the 75% resistance criterion, and the superconducting transition width $\Delta T_c = 0.23$ K, determined as the temperature interval between 10% and 90% of the resistance at 7 K. Application of a magnetic

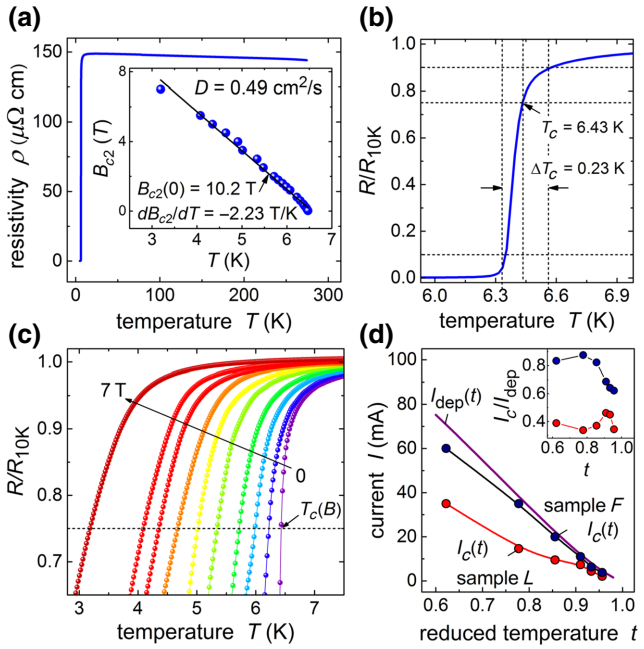

FIG. 2. Superconducting properties of the films. (a) Temperature dependence of the resistivity of sample L. Inset: temperature dependence of the upper critical field (symbols) of sample L fitted to the expression $B_{c2}(T) = B_{c2}(0)/0.7 - (dB_{c2}/dT)T$ (solid line). (b) Normalized resistance of sample L in the region of the superconducting transition. (c) Evolution of the superconducting transition of sample L with an increase of the magnetic field. (d) Temperature dependence of the experimentally measured critical current $I_c(t)$ (symbols) for both samples in comparison with the Ginzburg-Landau depairing current calculated by Eq. (1) (solid line). Inset: ratio $I_c/I_{\rm dep}$ for both samples versus reduced temperature t.

field leads to a broadening of the transition, accompanied by its systematic shift toward lower temperatures [see Fig. 2(c)]. Near T_c, the temperature dependence of the upper critical field $B_{c2}(T)$ exhibits a slope $dB_{c2}/dT = -2.23$ T/K, whose extrapolation toward zero temperature yields $B_{c2}(0) \approx 10.2$ T [see the inset in Fig. 2(a)]. This slope corresponds to an electron diffusion coefficient D of 0.49 cm^2/s, as deduced from the relation $D = -1.097(dB_{c2}/dT)^{-1}|_{T=T_c}$ [51]. The coherence length and the penetration depth at zero temperature are estimated [17] as $\xi(0) = \sqrt{\hbar D/(1.76 k_B T_c)} = 5.9$ nm and $\lambda(0) = 1.05 \times 10^{-3}\sqrt{\rho_{7\rm K}/T_c} \approx 495$ nm, with the Pearl length $\Lambda = 2\lambda^2(0)/d \approx 32$ μm. Thus, our strips are thin and wide, with $d \ll \lambda(0)$ and $\xi \ll \Lambda \lesssim W$.

III. RESULTS AND DISCUSSION

A. Critical current and current-voltage curves

The maximal value of the dissipation-free current I_c that the superconductor can carry is of primary importance for both its use in single-photon detectors and the realization of ultrafast vortex motion. Theoretically, at zero magnetic field, this current is given by the pair-breaking current $I_{\rm dep}$, whose temperature dependence can be described by the expression

$$I_{\rm dep}(T) = I_{\rm dep}(0)[1 - (T/T_c)^2]^{3/2},$$
$$\text{where} \quad I_{\rm dep}(0) = \frac{0.74 W[\Delta(0)]^{3/2}}{eR_\square \hbar D\sqrt{1 + W/(\pi\Lambda)}} \qquad (1)$$

for dirty superconductors [17,52,53]. In Eq. (1), $\Delta(0)$ is the superconducting gap at zero temperature, e the electron charge, and $R_\square$ the sheet resistance. The factor $\sqrt{1/[1 + W/(\pi\Lambda)]}$, which is absent for narrow strips ($W \ll \Lambda$), takes into account the nonuniform current distribution in strips with $W \gtrsim \Lambda$ [54]. With the BCS ratio $\Delta(0) \approx 1.76 k_B T_c$ we obtain $I_{\rm dep}(0) \approx 144$ mA for our MoSi strips.

The theoretical dependence $I_{\rm dep}(T)$ calculated by Eq. (1) is compared with the experimentally measured $I_c(T)$ in Fig. 2(d). We use the 0.5-mV voltage criterion for the deduction of the critical current I_c from the I-V curves, as illustrated in Fig. 3. This criterion, which is above the noise level in our setup, corresponds to the lowest voltage at the foot of the zero-field resistance jump for sample F. Note that in the investigated temperature range $0.5 < t < 1$, where $t = T/T_c$ is the reduced temperature, I_c varies between $0.3I_{\rm dep}$ and $0.5I_{\rm dep}$ for sample L and between $0.6I_{\rm dep}$ and $0.9I_{\rm dep}$ for sample F [see the inset in Fig. 2(d)].

The I-V curves for both samples are presented in Fig. 3 for $T = 5$ K ($0.78T_c$). In Figs. 3(a) and 3(d), we label three distinct regimes in the I-V curves: (I) the flux-flow regime, (II) the FFI, and (III) the normal conducting regime. Figures 3(b) and 3(e) show in more detail the nonlinear conductivity regimes preceding the voltage jumps. The last points (A) before the jumps correspond to the instability current I^* related to the instability voltage V^*.

A comparison of the I-V curves for both samples suggests that sample L transits into the highly resistive state at noticeably smaller currents than sample F. Herewith, nonlinear upturns in the I-V curves at the foot of the instability jump occur in a broader range of currents for sample F. This behavior is illustrated by the evolution of the instability point A_L for sample L to the instability point A_F for sample F for the I-V curves taken at the same field of 69 mT in Figs. 3(b) and 3(e). The extended regime of nonlinear conductivity (I-B) for sample F is also seen in the dV/dI versus I representation in Figs. 3(c) and 3(f), as compared with the regime of almost linear conductivity (regime I for sample L and regime I-A for sample F) at smaller currents. In this way, at a given magnetic field magnitude, sample F exhibits larger V^* than sample L. This enhancement is most pronounced at low magnetic fields.

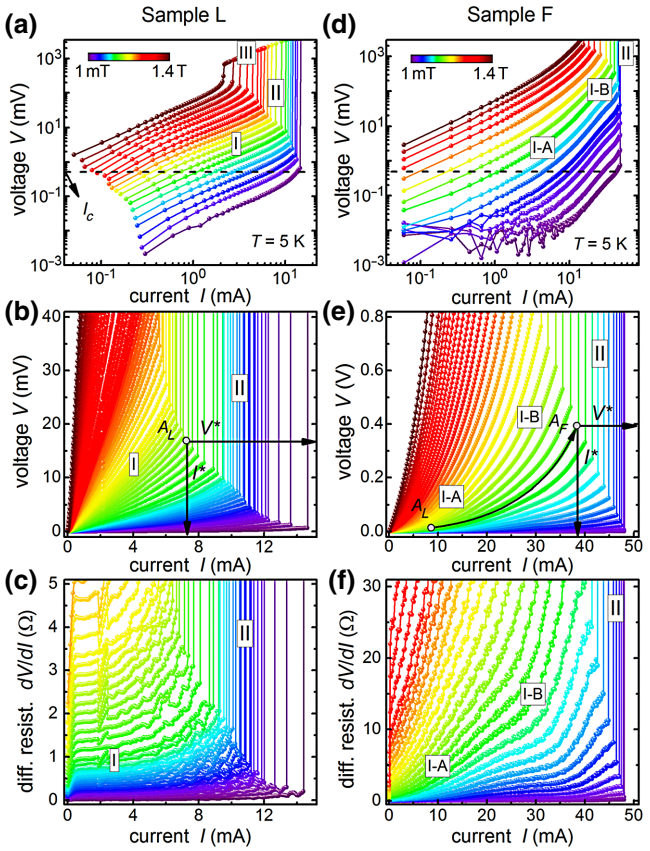

FIG. 3. I-V curves of the MoSi strips with (a)–(c) laser-etched edges (sample L) and (d)–(f) FIB-milled edges (sample F) at $T = 5$ K for a series of magnetic fields. (b),(e) Regimes of the nonlinear conductivity (I) and the flux-flow instability (II). The instability voltage V^* and current I^* are indicated for the I-V curves at $B = 69$ mT. (c),(f) Current dependences of the differential resistances.

B. Field dependence of the critical current

Magnetic field dependence of the critical current allows for the identification of various states the superconductor is passing with an increase of the magnetic field [5,54,55]. Namely, at low magnetic fields the sample can be in the vortex-free (Meissner) state, resulting in a linear decrease of $I_c(B)$. At higher fields, the decrease slows down, with a crossover at $B_{\rm stop}$ demarcating a transition to the mixed state [56]. In the Meissner state ($B < B_{\rm stop}$),

$$I_c(B) = I_c(0\ T)(1 - B/2B_{\rm stop}),$$
$$\text{where } B_{\rm stop} = \frac{\Phi_0\sqrt{1 + W/(\pi\Lambda)}}{2\sqrt{3}\pi\xi(T)W} \qquad (2)$$

contains the factor $\sqrt{1 + W/(\pi\Lambda)}$ because of the width $W \gtrsim \Lambda$. Equation (2) allows us to estimate $B_s = 2B_{\rm stop}$ as 0.3 mT for sample F. The physical meaning of B_s is the field value at which the surface barrier for vortex entry is suppressed at $I = 0$. The magnetic field dependence of the critical current for both samples is presented in Fig. 4(a). One can see that for sample F the theoretically calculated $B_{\rm stop} \sim 0.15$ mT is not very far from the experimental $B_{\rm stop} \sim 0.2$ mT and that the very steep decrease of $I_c(B)$ for sample F at $B \to 0$ [see the inset in Fig. 4(a)] could be an indication for a vortex-free state. Furthermore, the value of $I_c(0)$ for sample F is a factor of 3 larger than $I_c(0)$ for sample L, attesting to strong edge-barrier effects. For 1 mT $\leq B \leq$ 100 mT, $I_c(B)$ for sample F is described well by the dependence $I_c(B) = I_c(0\ T)B_{\rm stop}/(2B)$, indicating the dominating role of the edge barrier for vortex entry in sample F at $B \lesssim 100$ mT. In general, one could expect a slowing down towards the dependence $I_c(B) \sim B^{-0.5}$ in larger fields [5] because of the transition to the regime of dominating intrinsic (volume) pinning. Indeed, such a transition occurs at larger fields ($\backsimeq$ 300 mT, not shown) in sample F, pointing to the very small contribution of bulk pinning. This finding is in line with the high structural homogeneity of the amorphous MoSi films [see also Figs. 1(d) and 1(e)].

By contrast, in sample L, the dependence $I_c(B)$ is flattened at $B \lesssim 5$ mT. This behavior cannot be explained by a reduction of the edge barrier since the edge roughness leads only to a decrease of $I_c(0)$ and $B_{\rm stop}$ but not to

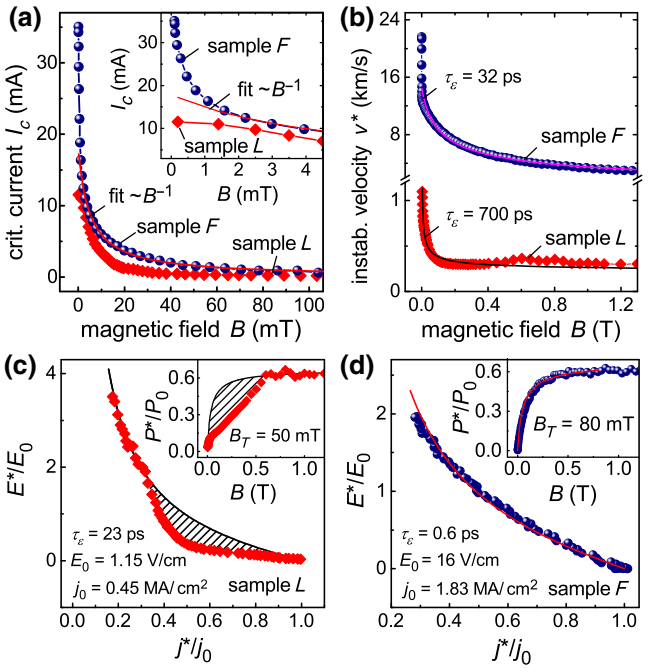

FIG. 4. (a) $I^*(B)$ for both samples. Symbols: experiment; lines: fits to Eq. (2). Inset: same $I_c(B)$ data at low fields. (b) $v^*(B)$ for both samples. Symbols: experiment; lines: fits to Eq. (3) with the energy relaxation time used as the only fitting parameter. (c),(d) Fits of the experimental data (symbols) to Eq. (6) (lines). The hatched area in (c) emphasizes the range of deviation of the experimental data for sample L from the calculation. In all panels, $T = 5$ K.

the change of the functional dependence $I_c(B)$. We believe that this behavior is connected with the change of the structure of MoSi by the laser-beam impact, within a distance of about 2 μm from the edge, leading to a strong inhomogeneity of MoSi near the edge and the appearance of vortex pinning there. Some indication for the vortex pinning comes not only from the drastically different dependence of $I_c(B)$ in sample L in comparison with sample F, but also from the comparison of their I-V curves. Namely, Fig. 3(a) reveals an exponential shape of the I-V curves, which could be considered as an indication of vortex creep in the near-edge region of sample L.

C. Maximal vortex velocity

The magnetic field dependence of the maximal vortex velocity v^*, deduced by using the standard relation $v^* = V^*/(BL)$, is presented in Fig. 4(b). For both samples, $v^*(B)$ decreases with an increase of B, roughly following the $v^* \sim B^{-1/2}$ law. However, the v^* values differ substantially, with v^* for sample F being a factor of approximately 20 larger than for sample L in the whole range of magnetic fields. For instance, for sample F, v^* reaches approximately 13 km/s at 5 mT, decreases to approximately 7 km/s at 200 mT, and then slowly decreases to approximately 3 km/s at 1 T. At the same time, for sample L, $v^* \approx 800$ m/s at 5 mT, decreases to 300 m/s at 200 mT, and remains nearly constant with a further increase of the magnetic field.

According to LO, the instability velocity v^* is independent of the magnetic field. As was argued by Doettinger *et al.* [57], the discrepancy between the field-dependent experimental v^* and the field-independent theoretical v^* can be overcome by taking into account the magnetic field dependence of the vortex lattice parameter. Namely, the nonequilibrium electron distribution is spatially uniform only whilst $v^*\tau_\epsilon$ is larger than the intervortex distance a. This regime is realized at high magnetic fields, as is also in line with our data in Fig. 4(b), where an almost constant v^* is observed at $B \gtrsim 600$ mT. At smaller fields the system can be recovered to a spatially homogeneous state by allowing v^* to grow according to the increase of a with decrease of the applied magnetic field, $a = \sqrt{2\Phi_0/(\sqrt{3}B)}$, where Φ_0 is the magnetic flux quantum. The LO expression is then complemented [57] with the term $a/\sqrt{D\tau_\epsilon}$, yielding

$$v^* = \left[\frac{(1-t)^{1/2} D[14\zeta(3)]^{1/2}}{\pi\tau_\epsilon}\right]^{1/2}\left(1+\frac{a}{\sqrt{D\tau_\epsilon}}\right). \quad (3)$$

The fits of our experimental data to Eq. (3) are shown by solid lines in Fig. 4(b). Here, $v^*(B)$ is calculated while varying the energy relaxation time τ_ϵ as the only fitting parameter. Specifically, the fits shown in Fig. 4(b) are obtained with $\tau_{\epsilon L} = 700$ ps and $\tau_{\epsilon F} = 32$ ps. We note that the fit by Eq. (3) for sample L is rather poor. We attribute this to the strongly local character of FFI because of the rough edge, which cannot be accounted for by the "global" LO model [57].

By contrast, for sample F, Eq. (3) fits well the data, with exception of just a few points at fields below 2 mT. We assume that at low fields the number of vortices n in the film can be smaller than what follows from the estimate $n\Phi_0 = BS$ (B, magnetic flux density; S, film area). For a very small number of vortices, their penetration can happen at those places where the edge barrier is suppressed most. In the case of a very strong variation in the edge barrier suppression by individual defects, the vortices may penetrate predominantly via the "strongest" edge defect until the barrier is suppressed at other places.

The ratio $\tau_{\varepsilon L}/\tau_{\varepsilon F} \approx 22$ illustrates that the fits by Eq. (3), which is widely used in recent works [23,24], yield τ_ϵ differing by more than an order of magnitude for strips made from the same material, but differing by the edge quality.

D. Larkin-Ovchinnikov-Bezuglyj-Shklovskij (LOBS) model

The LO theory was generalized by Bezuglyj and Shklovskij (BS) [28] for a finite rate of heat removal from superconductor to substrate. Based on the heat balance equation, BS introduced a new field parameter, the overheating field B_T:

$$B_T = 0.374 k_B^{-1} e R_\square h \tau_\epsilon, \quad (4)$$

where k_B is the Boltzmann constant and h the heat removal coefficient. The parameter B_T separates the region of small fields $B \lesssim B_T$ at which heat removal is fast enough and the instability is of nonthermal nature from the region of large fields $B_T \lesssim B \lesssim 0.4B_{c2}$ with insufficient heat removal and the heating mechanism dominating the instability. BS derived a scaling law for the electric field strength E^* and the current density j^* at the instability point:

$$\frac{E^*}{E_0} = [1 - f(b)]\left(\frac{j^*}{j_0}\right)^{-1}, \quad (5)$$

where E_0, j_0, and f are defined as

$$\begin{aligned} E_0 &= 1.02 B_T (D/\tau_\epsilon)^{1/2}(1-t)^{1/4}, \\ j_0 &= 2.62(\sigma_n/e)(D\tau_\epsilon)^{-1/2} k_B T_c (1-t)^{3/4}, \\ f &= [1 + b + (b^2 + 8b + 4)^{1/2}]/3(1+2b), \end{aligned} \quad (6)$$

with the reduced magnetic field $b = B/B_T$ and the normal state conductivity σ_n. If one fits the entirety of the experimentally deduced instability points $(E^*/E_0)(j^*/j_0)$ to Eq. (6), then the field dependence of the power density at the

instability point, $P_0 \equiv E_0 j_0 = h/d(T_c - T)$, allows one to deduce the overheating field B_T and the heat removal coefficient h. Substitution of h and B_T into Eq. (4) yields then the relaxation time τ_ϵ.

The best fits of the experimental data to Eq. (6) for both samples are presented in Figs. 4(c) and 4(d). For sample L the fit is very poor since in the range of currents $0.4 \lesssim (j^*/j_0) \lesssim 0.8$ the experimental data strongly deviate below the curve calculated by Eq. (6) [see the hatched area in Fig. 4(c)]. The fit in Fig. 4(c) is done with $E_0 = 1.15$ V/cm and $j_0 = 0.45$ MA/cm^2, yielding $B_T = 50$ mT, $h = 0.54$ W/(K cm^2), and $\tau_\varepsilon = 23$ ps. For sample F the fit is almost perfect as the experimental data fall onto the curve calculated by Eq. (6) in the entire range of magnetic fields. The fit in Fig. 4(d) is done with $E_0 = 16$ V/cm and $j_0 = 1.83$ MA/cm^2, yielding $B_T = 80$ mT, $h = 32.7$ W/(K cm^2), and $\tau_\varepsilon = 0.6$ ps. If one associates τ_ϵ with the electron-phonon scattering time $\tau_{e\text{-ph}}$ in the LO model [27], the deduced τ_ϵ is at least 1 order of magnitude smaller than one could expect from τ_ϵ found in similar low-T_c highly disordered superconductors [58–62]. We note that the LO theory was developed neglecting the diffusion term in the kinetic equation. This approximation is justified when the intervortex distance a is smaller than the quasiparticle diffusion length $l_\varepsilon = \sqrt{D\tau_\varepsilon}$, with $l_{\varepsilon L} \approx 34$ nm and $l_{\varepsilon F} \approx 7$ nm, suggesting that the deduced τ_ϵ values can hardly be treated even as order-of-magnitude estimates.

At present it is impossible to deduce the relaxation time from single-photon detection experiments directly. However, this can be done from, e.g., magnetoconductance measurements [60–62]. While for WSi, NbN, and NbTiN experiments yield the electron-phonon relaxation times on the sub-100-ps time scale [60–62], we are not aware of similar measurements for MoSi. Given the similarity of these highly disordered superconductors, we would expect that the relaxation time in MoSi is also on the sub-100-ps time scale.

In all, the results of our comparison of the experimental data with the LO and LOBS models can be summarized as follows. The LO model gives a strongly overestimated result ($\tau_{\varepsilon L} = 700$ ps) for sample L, while a rather expected relaxation time value ($\tau_{\varepsilon F} = 32$ ps) is obtained for sample F. By contrast, the LOBS model poorly describes FFI in sample L and gives an unrealistically small relaxation time for sample F ($\tau_{\varepsilon F} \simeq 0.6$ ps). It is important to stress that neither of these models takes into account the *local* character of FFI. Apparently, this explains the inapplicability of these models for sample L, which has a rough edge. In sample F, according to the edge-controlled instability theory (which includes heating effects) [7], FFI also nucleates at the edge. However, this model implies that the vortices should also move at a relatively high velocity in the film interior (otherwise FFI will not occur) and this links the results of the edge-controlled instability model [7] with the LO model [26,27]. This circumstance might explain the reasonable value for the relaxation time following from the LO model for sample F.

E. Numerical modeling

To get further insights into the spatiotemporal evolution of the order parameter in the strips with and without edge defects, we numerically solve the modified time-dependent Ginzburg-Landau (TDGL) equation in conjunction with the heat balance equation. The essential equations and the considered boundary conditions are detailed in the Appendix.

The shapes of the edges of sample L are unknown and their exact modeling is not feasible with currently available computation capabilities. Therefore we consider the effects of single edge defects of different shapes and an array of defects located near the edge of the strip. The defects are simulated as regions with a locally suppressed critical temperature.

The results of TDGL simulations for a single defect are presented in Fig. 5. Figure 5(a) presents the I-V curves calculated for the vortex entry through the edge containing a single, semicircle-shaped edge defect in comparison with the I-V curve for the vortex entry through the perfectly straight edge of the same strip. The simulations suggest that the low-dissipative regime of nonlinear conductivity extends toward larger currents (and, hence, higher vortex velocities) for the vortex entry via the perfect edge [point A' in Fig. 5(a)]. The spatial dependences of the superconducting order parameter at the last points before the instability jumps are illustrated in Fig. 5(b). Panel A in Fig. 5(b) illustrates the case when vortices enter via the edge containing a semicircle-shaped defect, while panel A' illustrates the case when they enter via the opposite smooth edge. The influence of the edge defect on the vortex dynamics is twofold. First, due to the current-crowding effect the defect suppresses the edge barrier for the penetration of vortices, turning the defect into the place of nucleation of vortex rivers [7]. Such vortex rivers represent self-organized Josephson-like junctions formed by chains of fast-moving vortices, which eventually evolve to normal domains expanding across the entire sample upon its abrupt transition to the highly resistive state. Second, the local deflection of the current flow direction from the y axis [see Fig. 1(a)] near the defect leads to the deviation of the Lorentz force direction and, hence, the direction of vortex motion from the x axis. As a result, a diverging "jet" of vortices is formed, as indicated by the dashed lines in panel A in Fig. 5(b).

By contrast, when vortices enter via the perfect edge [panel A' in Fig. 5(b)], the only effect that remains in comparison with the previously considered case is the local enhancement of the current density near the edge defect.

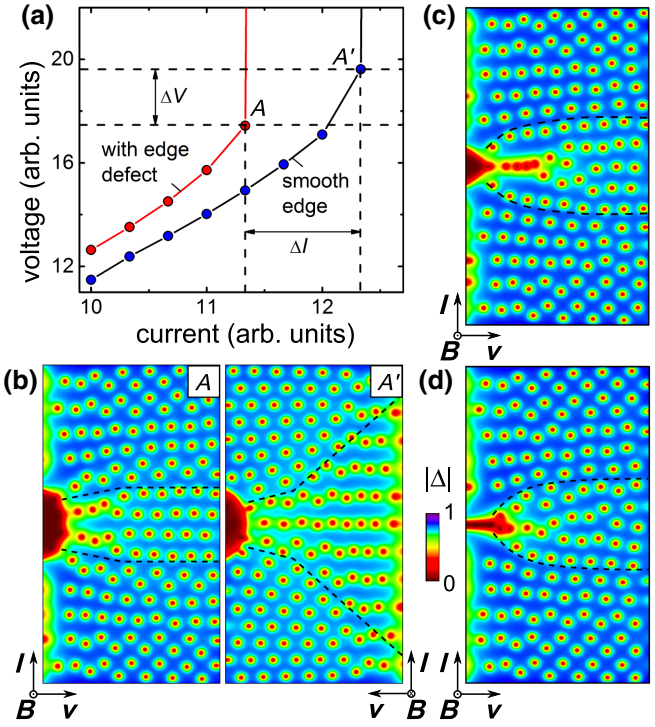

FIG. 5. (a) I-V curves calculated by the numerical solution of the TDGL equation for a superconducting strip with width $W = 100\xi_c$ at $T = 0.8T_c$ for $B = 0.05B_0$ for the vortex entry via the edge with a defect and via the (opposite) smooth edge. (b) Snapshots of the superconducting order parameter $|\Delta|$ are shown at the different current values $I/I_{\rm dep} = 0.34$ (point A) and $I/I_{\rm dep} = 0.37$ (point A'), corresponding to the instability points in (a). Dashed lines demarcate the regions of nucleation and evolution of vortex rivers. (c),(d) Nucleation of vortex jets (branched vortex rivers) upon vortex entry through an edge defect. For the studied system, the parameter $B_0 = \Phi_0/(2\pi\xi_c^2) \simeq 4.9$ T, where $\xi_c = \sqrt{1.76}\xi(0) = 7.8$ nm.

Panel A' in Fig. 5(b) shows that the nucleation of vortex rivers occurs at many different points along the perfect edge, while only those nucleated at the edge in front of the defect develop faster because of the larger current density. Figures 5(c) and 5(d) illustrate the development of vortex "jets" upon vortex entry via the edge containing a triangle-shaped and a slit-shaped defect.

The simulations also allow us to explain the role of a single defect in the FFI observed in Ref. [5]. As in that experiment, our model gives a several-percent suppression of I^* and V^* when vortices enter via an edge of the strip containing a defect compared with entry through the smooth edge, while I_c can be suppressed by more than 2 times (depending on the size and shape of the defect). That experimental observation [5] follows from the considered model, where FFI starts near the edge because of the higher local current density j and the electronic temperature T_e, but in the rest of the strip the vortices have to move at a large enough velocity to allow for the appearance of vortex rivers [63]. Thus, the edge defect increases j and T_e in comparison with the strip with the smooth edge and it leads to smaller I^* and V^*, but their values do not change drastically since the change in the current distribution decays fast with an increase of the distance from the defect (approximately inversely proportional to the square of the distance).

In our experiment, the difference in I^* and V^* for samples L and F is several times larger. In comparison with Ref. [5], in our case the laser etching not only creates edge defects but it also changes the material composition of the close-to-edge regions. To take this into account in the simulations, we introduce randomly distributed defects (each defect has a size of $2\xi_c \times 2\xi_c$ with a locally suppressed T_c) in the close-to-edge region of width $25\xi_c$ for the strip with $W = 100\xi_c$. However, the results for this system are similar to the ones for the strip with a single edge defect, namely, a relatively small suppression of I^* and V^* while the critical current could be suppressed significantly (as in the case of a single defect).

A comparison of the experimental results for samples L and F implies that FFI appears first in the close-to-edge region of sample L with width 2 μm $\ll$ 182 μm (which is inhomogeneous due to the laser etching) and only then does the FFI spread to the rest of the superconducting strip. Unfortunately, our model does not describe this process. We also try to simulate the initial FFI by introducing a local increase of the escape time $\tau_{\rm esc}$ of nonequilibrium phonons to the substrate in the close-to-edge region. Specifically, $\tau_{\rm esc}$ is larger by an order of magnitude in the region with width $25\xi_c$ for a strip with $W = 100\xi_c$. Indeed, we find that in that region, FFI sets on first but it does not spread deep into the strip, because of the cooling of the close-to-edge regions via diffusion of hot electrons to the neighboring regions. We note that the so-called healing length at the chosen parameters in our simulations is much larger than the length of penetration of the electric field. Whether it plays an important role or does not for spreading of the normal region into the interior of the strip should be clarified in further investigations.

IV. CONCLUSION

To sum up, we have investigated the effects of edge quality on the critical current and maximal vortex velocities in wide thin films of MoSi. The edges of different quality are produced by laser etching (sample L) and milling by a focused ion beam (sample F). The smooth edges in sample F allow for (i) a factor of about 3 increase of the zero-field critical current, (ii) a factor of 20 enhancement of the maximal vortex velocity up to about 20 km/s, and (iii) a factor of 20 smaller estimate for the energy relaxation time on the 30-ps time scale.

Our results have the following implications for superconducting devices. First, the enhancement of the current-carrying capability of the strips is relevant for SMSPDs. Namely, to achieve the theoretically predicted intrinsic detection efficiency of about 100%, SMSPDs should be biased by close-to-depairing critical currents [21]. In particular, in the MoSi strips with FIB-milled edges at 5 K, the zero field critical current has increased by a factor of 3, reaching 87% of the Ginzburg-Landau pair-breaking current. Second, the improvement of the current-carrying capability allows for the enhancement of the maximal vortex velocity, providing access to the previously inaccessible regimes (in this material) of generation of sound and spin waves via a Cherenkov-type mechanism [14–16], with a rich physics of fluxon-phonon and fluxon-magnon interactions [13,64]. From the viewpoint of basic research, our findings could be relevant for a possible explanation of the inconsistency between the (sub-)nanosecond relaxation times deduced from current-voltage measurements for many dirty superconductors, despite their potential (or already proven) capability of single-photon counting [23–25,36–38].

In all, our findings suggest the edge quality check as a route to improvement of the critical current in superconducting microstrip single-photon detectors and imply that homogeneous, dirty-limit superconductors with weak pinning should generally allow for ultrafast vortex motion at velocities exceeding 10 km/s. In particular, our results imply that for strips where no care is taken about the edge quality and the magnetic field dependence of the critical current does not attest to the dominating edge pinning of vortices, the flux-flow instability only allows for the deduction of some "indicative" relaxation time exceeding the intrinsic τ_ε in the material.

ACKNOWLEDGMENTS

The authors thank Roland Sachser for support with the nanofabrication. B.B. and B.A. acknowledge financial support by the Vienna Doctoral School in Physics (VDSP). D.Y.V. acknowledges support by the Russian Foundation for Basic Research (RFBR), Grant No. 18-29-20100. M.Yu.M. acknowledges partial support by the NAS of Ukraine through Grant No. 2/22-H. Support through the Frankfurt Center of Electron Microscopy (FCEM) and by the European Cooperation in Science and Technology via COST Actions CA16218 (NANOCOHYBRI) and CA19108 (HiSCALE) is gratefully acknowledged. M. Yu. M. acknowledges partial support by the NAS of Ukraine through Grant No. 2/22-H, and the WPI Scholarship within the framework of the Pauli Ukraine Project. This research is funded in whole, or in part, by the Austrian Science Fund (FWF), Grant No. I4865-N. For the purpose of open access, the authors have applied a CC BY public copyright license to any Author Accepted Manuscript version arising from this submission.

APPENDIX

Simulation results presented in Fig. 5 rely upon the solution of the modified TDGL equation [21]:

$$\frac{\pi\hbar}{8k_BT_c}\left(\frac{\partial}{\partial t}+\frac{2ie\varphi}{\hbar}\right)\Delta = \xi_{\rm mod}^2\left(\nabla - i\frac{2e}{\hbar c}A\right)^2\Delta + \left(1-\frac{T_e}{T_c}-\frac{|\Delta|^2}{\Delta_{\rm mod}^2}\right)\Delta + i\frac{({\rm div}\mathbf{j}_s^{\rm Us}-{\rm div}\mathbf{j}_s^{\rm GL})}{|\Delta|^2}\frac{e\Delta\hbar D}{\sigma_n\sqrt{2}\sqrt{1+T_e/T_c}},$$

where $\xi_{\rm mod}^2=\pi\sqrt{2}\hbar D/(8k_BT_c\sqrt{1+T_e/T_c})$, A is the vector potential, φ is the electrostatic potential, D is the diffusion coefficient, $\Delta_{\rm mod}^2=[\Delta_0\tanh(1.74\sqrt{T_c/T_e-1})]^2/(1-T_e/T_c)$, $\sigma_n=2e^2DN(0)$ is the normal-state conductivity, $N(0)$ is the single-spin density of states at the Fermi level, and $\mathbf{j}_s^{\rm Us}$ and $\mathbf{j}_s^{\rm GL}$ are the superconducting current densities in the Usadel and Ginzburg-Landau models:

$$\mathbf{j}_s^{\rm Us}=\frac{\pi\sigma_n}{2e\hbar}|\Delta|\tanh\left(\frac{|\Delta|}{2k_BT_e}\right)\mathbf{q}_s,$$

where $\mathbf{q}_s=\nabla\phi-2e\mathbf{A}/\hbar c$, ϕ is the phase of $\Delta=|\Delta|e^{i\phi}$, and

$$\mathbf{j}_s^{\rm GL}=\frac{\pi\sigma_n|\Delta|^2}{4e\hbar k_BT_c}\mathbf{q}_s.$$

At T_e not very close to T_c, the Ginzburg-Landau expression for the superconducting current is not valid quantitatively and one needs to use the Usadel expression for $\mathbf{j}_s^{\rm Us}$. In this case the TDGL equation should also be modified since the ordinary TDGL equation leads to ${\rm div}\mathbf{j}_s^{\rm GL}=0$ in the stationary case, while one needs ${\rm div}\mathbf{j}_s^{\rm Us}=0$. Accordingly, by adding the term ${\rm div}(\mathbf{j}_s^{\rm Us}-\mathbf{j}_s^{\rm GL})$ in the TDGL equation one provides ${\rm div}\mathbf{j}_s^{\rm Us}=0$. At $T_e\to T_c$ the modified TDGL equation reduces to the ordinary TDGL equation and ${\rm div}(\mathbf{j}_s^{\rm Us}-\mathbf{j}_s^{\rm GL})$ goes to zero.

The electron and phonon temperatures, T_e and T_p, respectively, are found from the solution of the following equations:

$$\frac{\partial}{\partial t}\left(\frac{\pi^2k_B^2N(0)T_e^2}{3}-\mathcal{E}_0\mathcal{E}_s(T_e,|\Delta|)\right) = \nabla k_s\nabla T_e-\frac{96\zeta(5)N(0)k_B^2}{\tau_0}\frac{T_e^5-T_p^5}{T_c^3}+jE,$$

$$\frac{\partial T_p^4}{\partial t}=-\frac{T_p^4-T^4}{\tau_{\rm esc}}+\gamma\frac{24\zeta(5)}{\tau_0}\frac{15}{\pi^4}\frac{T_e^5-T_p^5}{T_c},$$

where $\mathcal{E}_0=4N(0)(k_BT_c)^2$, $\mathcal{E}_0\mathcal{E}_s(T_e,|\Delta|)$ is the change in the energy of electrons due to the transition to the

superconducting state, k_s is the heat conductivity in the superconducting state,

$$k_s = k_n \left(1 - \frac{6}{\pi^2 (k_B T_e)^3} \int_0^{|\Delta|} \frac{\epsilon^2 e^{\epsilon/k_B T_e} d\epsilon}{(e^{\epsilon/k_B T_e} + 1)^2}\right),$$

$k_n = 2D\pi^2 k_B^2 N(0) T_e/3$ is the heat conductivity in the normal state, the term jE describes Joule dissipation, and $\tau_{\rm esc}$ is the escape time of nonequilibrium phonons to the substrate. The parameter γ is defined as $\gamma = (8\pi^2/5)[C_e(T_c)/C_p(T_c)]$, where $C_e(T_c)$ and $C_p(T_c)$ are the heat capacities of electrons and phonons at $T = T_c$, and the characteristic time τ_0 controls the strength of the electron-phonon and phonon-electron scattering [21]. Values of the parameters $\gamma = 9$ and $\tau_0 = 925$ ns used in the calculations are estimates for NbN. Their variation only leads to quantitative changes in the I-V curves.

The current continuity equation $\mathrm{div}(\mathbf{j}_s^{\rm Us} + \mathbf{j}_n) = 0$ is solved to find the electrostatic potential. Here, $\mathbf{j}_n = -\sigma_n \nabla\varphi$ is the normal current density. At the edges where vortices enter and exit the microstrip we use the boundary conditions $\mathbf{j}_n|_n = \mathbf{j}_s|_n = 0$ and $\partial T_e/\partial n = 0$, $\partial|\Delta|/\partial n = 0$ while at the edges along the current direction $T_e = T$, $|\Delta| = 0$, $\mathbf{j}_s|_n = 0$, $\mathbf{j}_n|_n = I/(wd)$. The latter boundary conditions model the contact of the superconducting strip with a normal reservoir being in equilibrium. This choice provides a way "to inject" the current into the superconducting microstrip in the modeling. The modeled length of the microstrip is $L = 4w$.

[1] L. Embon, Y. Anahory, Ž. L. Jelić, E. O. Lachman, Y. Myasoedov, M. E. Huber, G. P. Mikitik, A. V. Silhanek, M. V. Milošević, A. Gurevich, and E. Zeldov, Imaging of super-fast dynamics and flow instabilities of superconducting vortices, Nat. Commun. **8**, 85 (2017).

[2] V. Rouco, M. Massarotti, D. Stornaiuolo, G. P. Papari, X. Obradors, T. Puig, F. Tafuri, and A. Palau, Vortex lattice instabilities in $YBa_2Cu_3O_{7-x}$ nanowires, Materials **11**, 211 (2018).

[3] O. V. Dobrovolskiy, V. M. Bevz, E. Begun, R. Sachser, R. V. Vovk, and M. Huth, Fast Dynamics of Guided Magnetic Flux Quanta, Phys. Rev. Appl. **11**, 054064 (2019).

[4] A. Leo, A. Nigro, V. Braccini, G. Sylva, A. Provino, A. Galluzzi, M. Polichetti, C. Ferdeghini, M. Putti, and G. Grimaldi, Flux flow instability as a probe for quasiparticle energy relaxation time in Fe-chalcogenides, Supercond. Sci. Technol. **33**, 104005 (2020).

[5] O. V. Dobrovolskiy, D. Yu Vodolazov, F. Porrati, R. Sachser, V. M. Bevz, M. Yu Mikhailov, A. V. Chumak, and M. Huth, Ultra-fast vortex motion in a direct-write Nb-C superconductor, Nat. Commun. **11**, 3291 (2020).

[6] S. S. Ustavschikov, M. Yu. Levichev, I. Yu. Pashenkin, A. M. Klushin, and D. Yu. Vodolazov, Approaching depairing current in dirty thin superconducting strip covered by low resistive normal metal, Supercond. Sci. Technol. **34**, 015004 (2020).

[7] D. Yu. Vodolazov, Flux-flow instability in a strongly disordered superconducting strip with an edge barrier for vortex entry, Supercond. Sci. Technol. **32**, 115013 (2019).

[8] Alexei I. Bezuglyj, Valerij A. Shklovskij, Ruslan V. Vovk, Volodymyr M. Bevz, Michael Huth, and Oleksandr V. Dobrovolskiy, Local flux-flow instability in superconducting films near T_c, Phys. Rev. B **99**, 174518 (2019).

[9] V. G. Kogan and R. Prozorov, Interaction between moving Abrikosov vortices in type-II superconductors, Phys. Rev. B **102**, 024506 (2020).

[10] W. P. M. R. Pathirana and A. Gurevich, Nonlinear dynamics and dissipation of a curvilinear vortex driven by a strong time-dependent Meissner current, Phys. Rev. B **101**, 064504 (2020).

[11] V. G. Kogan and N. Nakagawa, Current distributions by moving vortices in superconductors, Phys. Rev. B **103**, 134511 (2021).

[12] W. P. M. R. Pathirana and A. Gurevich, Effect of random pinning on nonlinear dynamics and dissipation of a vortex driven by a strong microwave current, Phys. Rev. B **103**, 184518 (2021).

[13] B. I. Ivlev, S. Mejía-Rosales, and M. N. Kunchur, Cherenkov resonances in vortex dissipation in superconductors, Phys. Rev. B **60**, 12419 (1999).

[14] L. N. Bulaevskii and E. M. Chudnovsky, Sound generation by the vortex flow in type-II superconductors, Phys. Rev. B **72**, 094518 (2005).

[15] A. A. Bespalov, A. S. Mel'nikov, and A. I. Buzdin, Magnon radiation by moving Abrikosov vortices in ferromagnetic superconductors and superconductor-ferromagnet multilayers, Phys. Rev. B **89**, 054516 (2014).

[16] O. V. Dobrovolskiy, Q. Wang, D. Yu. Vodolazov, B. Budinska, R. Sachser, A. V. Chumak, M. Huth, and A. I. Buzdin, Cherenkov radiation of spin waves by ultra-fast moving magnetic flux quanta, arXiv:2103.10156 (2021).

[17] Yu. P. Korneeva, D. Yu. Vodolazov, A. V. Semenov, I. N. Florya, N. Simonov, E. Baeva, A. A. Korneev, G. N. Goltsman, and T. M. Klapwijk, Optical Single-Photon Detection in Micrometer-Scale NbN Bridges, Phys. Rev. Appl. **9**, 064037 (2018).

[18] Yu. P. Korneeva, N. N. Manova, I. N. Florya, M. Yu. Mikhailov, O. V. Dobrovolskiy, A. A. Korneev, and D. Yu. Vodolazov, Different Single-Photon Response of Wide and Narrow Superconducting Mo_xSi_{1-x} Strips, Phys. Rev. Appl. **13**, 024011 (2020).

[19] I. Charaev, Y. Morimoto, A. Dane, A. Agarwal, M. Colangelo, and K. K. Berggren, Large-area microwire MoSi single-photon detectors at 1550 nm wavelength, Appl. Phys. Lett. **116**, 242603 (2020).

[20] J. Chiles, S. M. Buckley, A. Lita, V. B. Verma, J. Allmaras, B. Korzh, M. D. Shaw, J. M. Shainline, R. P. Mirin, and S. W. Nam, Superconducting microwire detectors based on WSi with single-photon sensitivity in the near-infrared, Appl. Phys. Lett. **116**, 242602 (2020).

[21] D. Yu. Vodolazov, Single-Photon Detection by a Dirty Current-Carrying Superconducting Strip Based on the Kinetic-Equation Approach, Phys. Rev. Appl. **7**, 034014 (2017).

[22] M. Caputo, C. Cirillo, and C. Attanasio, NbRe as candidate material for fast single photon detection, Appl. Phys. Lett. **111**, 192601 (2017).

[23] J. A. Hofer and N. Haberkorn, Flux flow velocity instability and quasiparticle relaxation time in nanocrystalline β-W thin films, Thin Sol. Films **730**, 138690 (2021).

[24] Z. Liu, B. Luo, L. Zhang, B. Hou, and D. Wang, Vortex dynamics in amorphous MoSi superconducting thin films, Supercond. Sci. Technol. (2021).

[25] C. Cirillo, V. Granata, A. Spuri, A. Di Bernardo, and C. Attanasio, NbReN: A disordered superconductor in thin film form for potential application as superconducting nanowire single photon detector, Phys. Rev. Mater. **5**, 085004 (2021).

[26] A. I. Larkin and Yu. N. Ovchinnikov, Nonlinear conductivity of superconductors in the mixed state, J. Exp. Theor. Phys. **41**, 960 (1976).

[27] A. I. Larkin and Y. N. Ovchinnikov, *Nonequilibrium Superconductivity* (Elsevier, Amsterdam, 1986), p. 493.

[28] A. I. Bezuglyj and V. A. Shklovskij, Effect of self-heating on flux flow instability in a superconductor near T_c, Physica C **202**, 234 (1992).

[29] A. V. Silhanek, A. Leo, G. Grimaldi, G. R. Berdiyorov, M. V. Milošević, A. Nigro, S. Pace, N. Verellen, W. Gillijns, V. Metlushko, B. Ilić, X. Zhu, and V. V. Moshchalkov, Influence of artificial pinning on vortex lattice instability in superconducting films, New J. Phys. **14**, 053006 (2012).

[30] V. A. Shklovskij, A. P. Nazipova, and O. V. Dobrovolskiy, Pinning effects on self-heating and flux-flow instability in superconducting films near T_c, Phys. Rev. B **95**, 184517 (2017).

[31] O. V. Dobrovolskiy, V. A. Shklovskij, M. Hanefeld, M. Zörb, L. Köhs, and M. Huth, Pinning effects on flux flow instability in epitaxial Nb thin films, Supercond. Sci. Technol. **30**, 085002 (2017).

[32] O. V. Dobrovolskiy, C. González-Ruano, A. Lara, R. Sachser, V. M. Bevz, V. A. Shklovskij, A. I. Bezuglyj, R. V. Vovk, M. Huth, and F. G. Aliev, Moving flux quanta cool superconductors by a microwave breath, Commun. Phys. **3**, 64 (2020).

[33] R. J. Watts-Tobin, Y. Krähenbühl, and L. Kramer, Nonequilibrium theory of dirty, current-carrying superconductors: Phase-slip oscillators in narrow filaments near Tc, J. Low Temp. Phys. **42**, 459 (1981).

[34] B. Korzh *et al.*, Demonstration of sub-3 ps temporal resolution with a superconducting nanowire single-photon detector, Nat. Photon. **14**, 250 (2020).

[35] C. Cirillo, J. Chang, M. Caputo, J. W. N. Los, S. Dorenbos, I. Esmaeil Zadeh, and C. Attanasio, Superconducting nanowire single photon detectors based on disordered NbRe films, Appl. Phys. Lett. **117**, 172602 (2020).

[36] A. V. Samoilov, M. Konczykowski, N. C. Yeh, S. Berry, and C. C. Tsuei, Electric-Field-Induced Electronic Instability in Amorphous Mo_3Si Superconducting Films, Phys. Rev. Lett. **75**, 4118 (1995).

[37] S. G. Doettinger, S. Kittelberger, R. P. Huebener, and C. C. Tsuei, Quasiparticle energy relaxation in the cuprate superconductors, Phys. Rev. B **56**, 14157 (1997).

[38] S.-Z. Lin, O. Ayala-Valenzuela, R. D. McDonald, L. N. Bulaevskii, T. G. Holesinger, F. Ronning, N. R. Weisse-Bernstein, T. L. Williamson, A. H. Mueller, M. A. Hoffbauer, M. W. Rabin, and M. J. Graf, Characterization of the thin-film NbN superconductor for single-photon detection by transport measurements, Phys. Rev. B **87**, 184507 (2013).

[39] A. V. Gurevich and R. G. Mints, Localized waves in inhomogeneous media, Sov.Phys. Usp. **27**, 19 (1984).

[40] A. I. Bezuglyj and V. A. Shklovskij, Thermal domains in inhomogeneous current-carrying superconductors. current-voltage characteristics and dynamics of domain formation after current jumps, J. Low Temp. Phys. **57**, 227 (1984).

[41] A. Buzdin and M. Daumens, Electromagnetic pinning of vortices on different types of defects, Physica C **294**, 257 (1998).

[42] A. Yu. Aladyshkin, A. S. Mel'nikov, I. A. Shereshevsky, and I. D. Tokman, What is the best gate for vortex entry into type-II superconductor?, Physica C **361**, 67 (2001).

[43] D. Y. Vodolazov, I. L. Maksimov, and E. H. Brandt, Vortex entry conditions in type-II superconductors: Effect of surface defects, Physica C **384**, 211 (2003).

[44] D. Cerbu, V. N. Gladilin, J. Cuppens, J. Fritzsche, J. Tempere, J. T. Devreese, V. V. Moshchalkov, A. V. Silhanek, and J. Van de Vondel, Vortex ratchet induced by controlled edge roughness, New J. Phys. **15**, 063022–1–13 (2013).

[45] J. R. Clem and K. K. Berggren, Geometry-dependent critical currents in superconducting nanocircuits, Phys. Rev. B **84**, 174510 (2011).

[46] G. P. Mikitik, Critical current in thin flat superconductors with Bean-Livingston and geometrical barriers, Phys. Rev. B **104**, 094526 (2021).

[47] M. Caloz, M. Perrenoud, C. Autebert, B. Korzh, M. Weiss, Ch. Schönenberger, R. J. Warburton, H. Zbinden, and F. Bussières, High-detection efficiency and low-timing jitter with amorphous superconducting nanowire single-photon detectors, Appl. Phys. Lett. **112**, 061103 (2018).

[48] Yu. P. Korneeva, M. Yu. Mikhailov, Yu. P. Pershin, N. N. Manova, A. V. Divochiy, Yu. B. Vakhtomin, A. A. Korneev, K. V. Smirnov, A. G. Sivakov, A. Yu. Devizenko, and G. N. Goltsman, Superconducting single-photon detector made of MoSi film, Supercond. Sci. Technol. **27**, 095012 (2014).

[49] O. V. Dobrovolskiy, M. Kompaniiets, R. Sachser, F. Porrati, Ch. Gspan, H. Plank, and M. Huth, Tunable magnetism on the lateral mesoscale by post-processing of Co/Pt heterostructures, Beilstein J. Nanotech. **6**, 1082 (2015).

[50] F. Porrati, S. Barth, R. Sachser, O. V. Dobrovolskiy, A. Seybert, A. S. Frangakis, and M. Huth, Crystalline niobium carbide superconducting nanowires prepared by focused ion beam direct writing, ACS Nano **13**, 6287 (2019).

[51] A. Semenov, B. Günther, U. Böttger, H.-W. Hübers, H. Bartolf, A. Engel, A. Schilling, K. Ilin, M. Siegel, R. Schneider, D. Gerthsen, and N. A. Gippius, Optical and transport properties of ultrathin NbN films and nanostructures, Phys. Rev. B **80**, 054510 (2009).

[52] J. Romijn, T. M. Klapwijk, M. J. Renne, and J. E. Mooij, Critical pair-breaking current in superconducting aluminum strips far below T_c, Phys. Rev. B **26**, 3648 (1982).

[53] John R. Clem and V. G. Kogan, Kinetic impedance and depairing in thin and narrow superconducting films, Phys. Rev. B **86**, 174521 (2012).

[54] B. L. T. Plourde, D. J. Van Harlingen, D. Yu. Vodolazov, R. Besseling, M. B. S. Hesselberth, and P. H. Kes, Influence of edge barriers on vortex dynamics in thin weak-pinning superconducting strips, Phys. Rev. B **64**, 014503 (2001).

[55] K. Ilin, D. Henrich, Y. Luck, Y. Liang, M. Siegel, and D. Yu. Vodolazov, Critical current of Nb, NbN, and TaN thin-film bridges with and without geometrical nonuniformities in a magnetic field, Phys. Rev. B **89**, 184511 (2014).

[56] G. M. Maksimova, Mixed state and critical current in narrow semiconducting films, Phys. Sol. Stat. **40**, 1607 (1998).

[57] S. G. Doettinger, R. P. Huebener, and A. Kühle, Electronic instability during vortex motion in cuprate superconductors regime of low and high magnetic fields, Physica C **251**, 285 (1995).

[58] D. Babić, J. Bentner, C. Sürgers, and C. Strunk, Flux-flow instabilities in amorphous $Nb_{0.7}Ge_{0.3}$ microbridges, Phys. Rev. B **69**, 092510–1–4 (2004).

[59] M. V. Sidorova, A. G. Kozorezov, A. V. Semenov, Yu. P. Korneeva, M. Yu. Mikhailov, A. Yu. Devizenko, A. A. Korneev, G. M. Chulkova, and G. N. Goltsman, Nonbolometric bottleneck in electron-phonon relaxation in ultrathin WSi films, Phys. Rev. B **97**, 184512 (2018).

[60] M. Sidorova, A. D. Semenov, H.-W. Hübers, S. Gyger, S. Steinhauer, X. Zhang, and A. Schilling, Magnetoconductance and photoresponse properties of disordered NbTiN films, Phys. Rev. B **104**, 184514 (2021).

[61] X. Zhang, A. Engel, Q. Wang, A. Schilling, A. Semenov, M. Sidorova, H.-W. Hübers, I. Charaev, K. Ilin, and M. Siegel, Characteristics of superconducting tungsten silicide W_xSi_{1-x} for single photon detection, Phys. Rev. B **94**, 174509 (2016).

[62] M. Sidorova, A. Semenov, H.-W. Hübers, K. Ilin, M. Siegel, I. Charaev, M. Moshkova, N. Kaurova, G. N. Goltsman, X. Zhang, and A. Schilling, Electron energy relaxation in disordered superconducting NbN films, Phys. Rev. B **102**, 054501 (2020).

[63] A. V. Silhanek, M. V. Milošević, R. B. G. Kramer, G. R. Berdiyorov, J. Van de Vondel, R. F. Luccas, T. Puig, F. M. Peeters, and V. V. Moshchalkov, Formation of Stripelike Flux Patterns Obtained by Freezing Kinematic Vortices in a Superconducting Pb Film, Phys. Rev. Lett. **104**, 017001 (2010).

[64] O. V. Dobrovolskiy, R. Sachser, T. Brächer, T. Böttcher, V. V. Kruglyak, R. V. Vovk, V. A. Shklovskij, M. Huth, B. Hillebrands, and A. V. Chumak, Magnon-fluxon interaction in a ferromagnet/superconductor heterostructure, Nat. Phys. **15**, 477 (2019).